ISSN 2447-6102

Article

Numerical analysis of an onshore oscillating water column wave energy converter for different wall slopes

Güths, A.K. [1], Teixeira, P.R.F.[1]* and Didier, E.[2]

[1] Universidade Federal do Rio Grande, Rio Grande, Brazil; guths@furg.br; pauloteixeira@furg.br
[2] Laboratório Nacional de Engenharia Civil, Lisboa, Portugal; edidier@lnec.pt

* Correspondence: pauloteixeira@furg.br

Received: 06/11/2020; Accepted: 05/12/2020; Published: 31/12/2020

Abstract: An alternative to the energy matrix expansion, due to the increase of global electricity demand, is the renewable sea wave energy source, which has high energy potential. The Oscillating Water Column (OWC) converter is one of the most studied, although it is not yet used at commercial scale. Therefore, searching the optimal geometric configuration is fundamental to turn this device viable. This study proposes a numerical analysis of an onshore OWC for different slopes of chamber walls (from 40^{o} to 90^{o}) and equipped with a Wells turbine. Simulations of incompressible 2D flows are performed by means of the FLUENT® software, which is based on Reynolds-averaged Navier-Stokes (RANS) equations. The *k-ε* turbulence model and the Volume of Fluid (VOF) method are employed. Analyses of the behavior of run up/down in the front wall, sloshing inside the chamber and the energy balance of the OWC are carried out for incident waves with periods from 6 to 12 s and height of 1.5 m. Chamber with wall slope of 40^{o} reaches the highest extracted energy (*EE)* at wave periods of 9 s and 10.5 s (70% of the incident wave energy) and higher run-up/down on the front wall and sloshing inside the chamber. However, chamber with wall slope of 90^{o} has more regularity of *EE* at the range of wave periods, which allows concluding that the choice of the optimal wall slope depends mainly on the sea state characteristics.

Keywords: oscillating water column; wave energy; renewable energy; numerical simulation.

1. Introduction

The global demand for electricity has increased over years. An increase of energy demand in approximately 200% at the next 30 years in Brazil is estimated, according to Costa et al. (2017). Therefore, alternative energy is a good option to contribute to this future requirement. Ocean waves are renewable energy source with high potential for supplying electricity, since the theoretical total energy potential of the waves is estimated in 32.000 TWh/year (Mørk et al., 2010). This potential is capable of supplying the current global consumption of electricity (26.730 TWh/year, according to IEA (2020)), which enables to be consider as a possible alternative energy.

When onshore Oscillating Water Column (OWC) wave converters are attached to breakwaters, they have some advantages, such as low construction and maintenance costs (Lisboa, 2016). The working principle of this converter is based on the action of incident waves in the OWC chamber, which impose the water flow to pass through a submerged opening; it causes free surface oscillations inside the chamber and, consequently, exhalation and inhalation of the air, which pass by a turbine that generates mechanical energy being converted into electrical energy (Lagoun et al., 2010).

Although several studies of the OWC device have been carried out, the power conversion performance of the OWC device is not yet attractive for its construction at commercial scale. Therefore, researches are still developed to optimize the efficiency of this system. The knowledge of the energy distribution due the interaction between the waves and the device is important to improve OWC designs. Some authors investigated the energy balance around OWC devices, such as Tseng et al. (2000), Folley and Whittaker (2002), Elhanafi et al. (2016) and Gaspar et al. (2020). The latter studied numerically the influence of the slope of walls of an OWC device considering two geometric

configurations, based on the Pico's plant, Azores, Portugal and LIMPET's, Isley Island, Scotland. In general, results of these authors showed that the device with the wall slope of 40° has better efficiency than the one of 90°.

This study aims expanding Gaspar et al.'s research in order to evaluate the performance of OWC devices with different wall slopes, from 40° to 90°. The hydro pneumatic behavior analyses and the energy balance are studied to understand several aspects of phenomena caused by the wave-structure interaction. Numerical analyses of onshore OWC devices (10 m long and 10 m wide) at the end of a flume 10 m deep with Wells turbines are carried out by means of the FLUENT® software (FLUENT, 2016), which is based on Reynolds-averaged Navier-Stokes (RANS) equations.

2. Materials and Methods

In this section, characteristics of case studies and the mathematical model are shown. Different types of energy and how they are monitored during simulations are also reported. Besides, the FLUENT® software is described, including their govern equations and methodology.

2.1 Case Studies

The case studies consist of the incidence of regular waves on onshore OWC devices with different wall slopes located at the end of a flume 10 m deep (Figure 1). Both length and width of the chambers are 10 m, the frontal wall is submerged in 2.5 m and the air chamber is 6 m high. These geometric characteristics are similar to those of Pico's plant and were adopted previously by Teixeira et al. (2013), Torres et al. (2016) and Gaspar et al. (2020) in their analyses. Considering that the chamber walls of OWC of Pico's plant are vertical (θ_2 = 90°) and the wall slope of LIMPET is θ_2 = 40°, different wall slopes, from 40° and 90°, are investigated: θ_2= 40°, 52°, 65°, 77° and 90°. Analyses are carried out for incident waves with periods of *T* = 6, 7.5, 9, 10.5, 12 s and height *H* = 1.5 m.

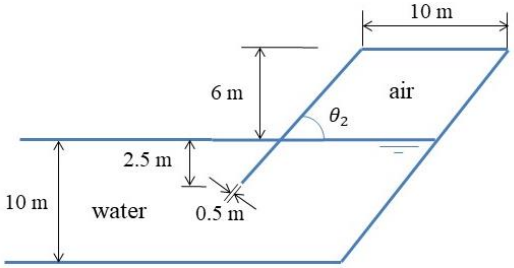

Figure 1. Scheme of case studies.

The turbine characteristic relation is the relation between the pressure drop Δp and the volumetric flow rate *Q*, expressed in Eq. (1).

$$\Delta p = kt\, Q \tag{1}$$

where Δ*p* is the difference between the air pressure inside the chamber and the atmospheric pressure. In this study, the Wells turbine has a turbine characteristic relation of *kt* = 100 Pa.s/m^3, which corresponds to approximately the optimal *kt* used in Pico's plant, whose Wells turbine had a diameter of 2.3 m (Falcão , 2002).

The pneumatic power (*P*) available to the Wells turbine can be calculated as follow (Torres et al., 2016):

$$P = \frac{\Delta p^2}{kt} \tag{2}$$

Analyzes of energy balance around the OWC device are carried out considering that the incident wave energy (*EI*) is distributed in extract energy (*EE*), reflected wave energy (*ER*) and energy losses (*EL*) (Gaspar et al., 2020). Therefore, the energy balance is given by

$$EI = ER + EE + EL \tag{3}$$

EI is calculated by Eq. (4), based on the linear wave theory (Dean and Dalrymple, 2000). *ER* depends on the reflected wave height (H_R), given by Eq. (5).

$$EI = \frac{1}{8}\rho g H^2 L b \tag{4}$$

$$ER = \frac{1}{8}\rho g H_R^2 L b \tag{5}$$

where ρ is the density of the water, g is the gravitational acceleration, H is the wave height, H_R is the reflected wave height, L is the wavelength and b is the chamber width (b = 10 m in this study).

EE is the time-averaged pneumatic energy *EE* extracted by the turbine, calculated by following:

$$EE = \int_0^T \Delta p(t) Q(t) dt \tag{6}$$

In this study, *EE* and *ER* are measured and *EI* is known theoretically; thus, *EL*, which is energy losses due to viscous forces and turbulence, is calculated by means of Eq. (3). The efficiency of the OWC device is the relation between *EE* and *EI*.

2.2 Mathematical model

Numerical simulations are performed by means of the FLUENT® software, in which the finite volume method is applied to the fluid dynamic equations. In this study, the flow is considered incompressible and two-dimensional, given by continuity and Navier-Stokes equations (Versteeg and Malalasekera, 1999):

$$\frac{\partial u_i}{\partial x_i} = 0 \tag{7}$$

$$\frac{\partial u_i}{\partial x_i} + u_j \frac{\partial u_i}{\partial x_j} = -\frac{1}{\rho}\frac{\partial p}{\partial x_i} + g_i + \frac{1}{\rho}\frac{\partial \tau_{ij}}{\partial x_j} \tag{8}$$

where i, j = 1, 2, ρ é the density, g_i are components of the gravitational acceleration, u_i are components of the velocity, p is the pressure, μ is the viscosity and τ_{ij} is the viscous stress tensor. For turbulent flows, the RANS equations are considered and the k- ε turbulence model is used to close the equations in this study. The Volume of Fluid method (VoF) is used to deal with the two-phase flow (water and air) and track the air-water interface. In this method, the volume fraction α (0 for air and 1 for water) is calculated by the transport equation:

$$\frac{\partial \alpha}{\partial t} + u_j \frac{\partial \alpha}{\partial x_j} = 0 \tag{9}$$

The computational domain is composed of a numerical flume 10 m deep and 2*L* long with the OWC device at its end (Figure 2). At each instant, the pressure calculated by Eq. (1) is imposed on the top boundary of the OWC chamber to consider the turbine drop. Velocity components and volume fraction are imposed at each instant on the wave maker, based on the second order Stokes wave theory (Dean and Dalrymple, 2000). An active absorption technique, proposed by Schäffer and Klopman (2000), is used to eliminate re-reflection of waves into the flume. The non-slip condition is imposed on the chamber walls and the bottom. The atmospheric pressure is applied to the top boundary of the wave flume. These boundary conditions are applied by means of User Defined Functions (UDF), whose methodology had validated and applied by several authors (Conde et al., 2011; Teixeira et al., 2013; Dias et al., 2015; Mendonça et al., 2018 and Gaspar et al., 2020).

The Gmsh software is used to build the regular meshes with quadrilateral cells. Figure 3 shows the mesh used for T = 6 s and θ_2 = 40°, in which there are refinements in the free surface zone and around the OWC chamber. Meshes have 70 cells per wavelength in the horizontal direction and 40 cells in the vertical direction of the free surface zone that has a height of 2*H*. Around the OWC walls, cells with 0.125 m in horizontal direction are used. This methodology was validated and applied by Teixeira et al. (2013) and Didier et al. (2016).

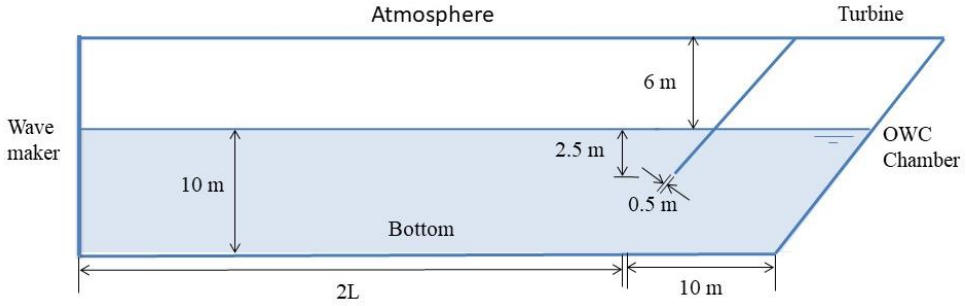

Figure 2. Computational domain and boundary conditions of the case with θ_2 = 40°.

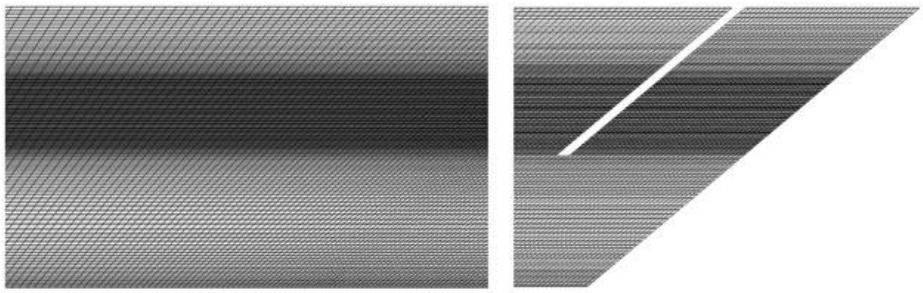

Figure 3. Detail of the mesh for the case with θ_2 = 40°, *T* = 9 s.

Gauges are located at the flume to determine the free surface position at each instant (Figure 4). Near the boundary of the front wall is located the gauge GWB to monitor run up/down. Gauges GC1, GC2 and GC3 are equidistant ones inside the chamber and GWA1 and GWA2 are near the internal boundary of the chamber walls; they allow determining the sloshing inside the chamber. The mean air pressure inside the air chamber is monitored by integrating the pressure in the chamber.

Gauge G1 monitors the free surface elevation near the wave maker. The reflection coefficient is determined by means of three gauges along the flume, GR1 at 1*L* from the wave maker, GR2 at 0.1*L* from the GR1 and GR3 at 0.27*L* from the GR1. The methodology implemented by Sousa et al. (2011), based on the algorithm developed by Mansard e Funke (1980) is applied to determine the reflection coefficient.

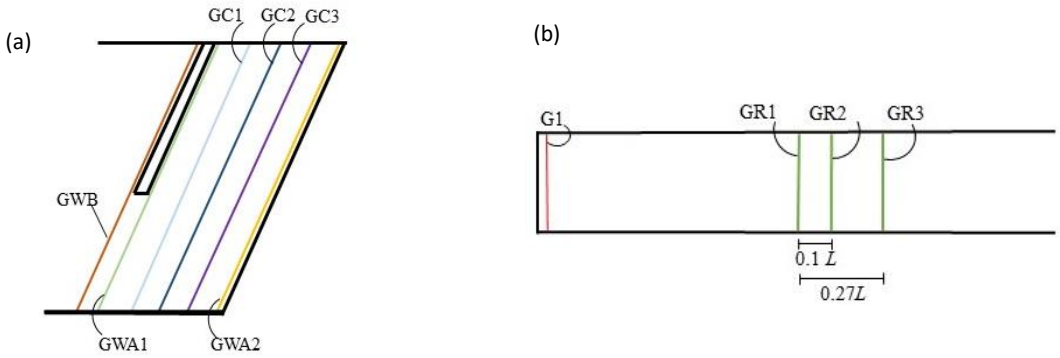

Figure 4. Scheme of gauges to determine: **(a)** run up/down, sloshing; and **(b)** reflection coefficient.

3. Results and discussion

In this section, analysis of the wave with *T*= 9 s and *H*= 1.5 m in a flume is carried out to verify the wave propagation process. Besides, the same incident wave is used to investigate the hydro-pneumatic behavior of OWC devices with wall slopes of 40° and 90°. Finally, analysis of the energy balance is shown to quantify types of energy distributed by the wave energy input into the flume.

3.1 Analysis of wave propagation

An analysis of the wave with *T*= 9 s and *H*= 1.5 m (intermediate period of the range) in a flume 10 m deep and 5*L* long (*L* = 81.7 m) is carried out to verify the wave propagation process. A second-order Stokes wave is imposed on the wave-maker. Besides, the active absorption technique is applied to the wave-maker and the end of the flume. Figure 5 shows time series of free surface elevations at 5 gauges along the flume, four of them are distant from the wave-maker of 1 m, 1*L*, 2.5*L*, 4*L*, and one gauge is at 1 m from the boundary of the end of the flume. They are compared with time series of the free surface elevation obtained theoretically (Dean and Dalrymple, 2000).

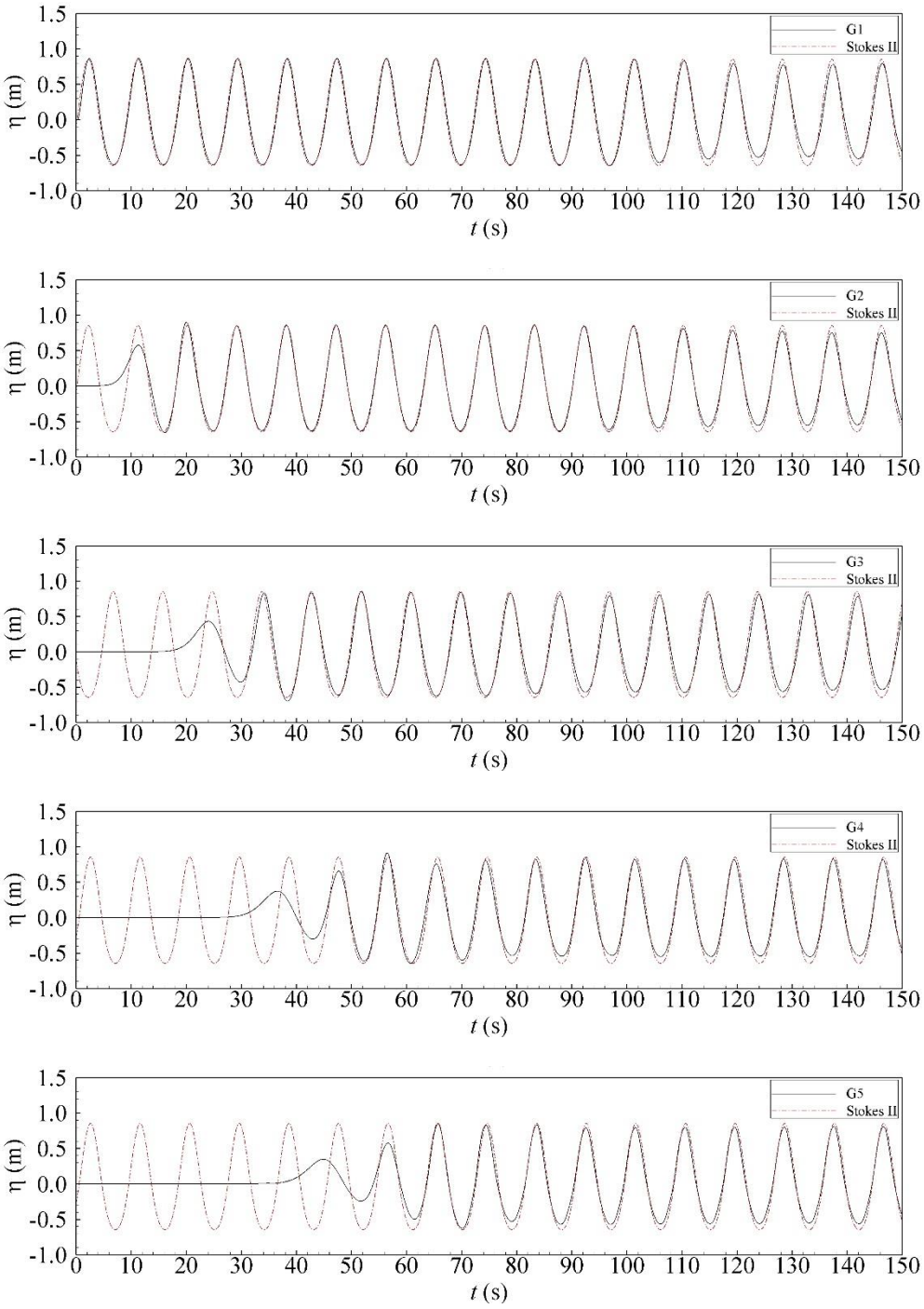

Figure 5. Time series of free elevations located at 1 m (G1), 1*L* (G2), 2.5*L* (G3) and 4*L* (G4) from the wave maker, 1 m from the end of the flume (G5); and the one of the theoretical second order-Stokes wave (Stokes II).

Table 1 shows percentage differences of the wave heights obtained at the gauges after the stabilization in relation to the theoretical one. These results show that numerical results are in good agreement with the theoretical one. Differences increase with the increase of the distance of the wave maker; however, they are still very low.

Therefore, wave generation and active absorption used in this study simulate accurately wave propagation in the flume.

Table 1. Percentage differences of the wave heights of gauges related to theoretical one

Gauges	G1	G2	G3	G4	G5
Dif. (%)	0.4	0.2	1.6	3.5	3.0

3.2 Analysis of the hydro-pneumatic behavior

The case of an incident wave with T = 9 s e H = 1.5 m is used to investigate the hydro-pneumatic behavior of OWC devices with wall slopes of 40° and 90° (vertical), which are the limits of the range of the wall slopes. Figure 6 (wall slope of 40°) and Figure 7 (wall slope of 90°) show contours of the velocity magnitude and streamlines at nine instants that complete one wave period, in which the first one (t = 0) corresponds to the zero-up crossing of the free surface elevation inside the chamber. Time series of the air pressure inside the chamber and the free surface at external surface of the frontal walls are shown in Figures 8 and 9, respectively, synchronized with images of Figures 6 and 7.

It is noticed that, at t = 0 (Figure 6), the water flow enters into the chamber and the air pressure inside the chamber is approximately null (Figure 8); the free surface elevation near the external surface of the frontal wall shows a run-up of 1.24 m (Figure 9). At instant t = 2T/8, the velocity magnitude is very low inside the chamber (around 0.20 m/s), due to the free surface is near of the maximum one, while its magnitude is high on the front wall (2.10 m/s) (Figure 6); the water flow is going out the chamber and the free surface on the front wall is descendent (free surface elevation equal to 0.84 m in Figure 9); the air pressure inside the chamber is the maximum one (5.77 kPa shown in Figure 8). At t = 4T/8 (Figure 6) a run-down phenomenon occurs at frontal wall (-0.99 m); the velocity magnitude is higher on the inferior part of the lip (2.10 m/s); the air pressure inside the chamber is almost null (Figure 8). At t = 6T/8 (Figure 6), the free surface inside the chamber is minimum and the velocity magnitude has low values (between 0.15 and 0.43 m/s); the air pressure is the minimum one (-5.77 kPa, shown in Figure 8); the flow of water is entering the chamber and the free surface on the front wall is rising (-0.41 m shown in Figure 9). At t = 8T/8 (Figure 6), the behavior is similar to that of instant t = 0, since this instant complete the analyzed cycle.

Contours of the velocity magnitude and streamlines at nine instants are also shown for the wall slope of 90° in Figure 7. It is noticed that, at t = 0, the behavior is similar to that the wall slope of 40° and the run-up is 1.20 m (Figure 9). At instant t = 2T/8 the velocity magnitude is low inside the chamber (around 0.30 m/s), and vortices occur near of the frontal wall (around 0.80 m/s); the air pressure inside the chamber is the maximum one (5.90 kPa, shown in Figure 8); and the free surface elevation on the front wall is 0.061 m (Figure 9). At t = 4T/8, a run-down phenomenon occurs at frontal wall (-0.52 m); the velocity magnitude is higher on the inferior part of the lip (1.40 m/s); the air pressure inside the chamber is almost null (Figure 8). At t = 6T/8, the free surface inside the chamber is minimum and the velocity magnitude has low values (around 0.08 m/s), and vortices occur near on the inferior part of the lip (between 0.12 and 0.40 m/s); the air pressure is the minimum one (-4.68 kPa).

The analysis of the run-up/down phenomenon is important to prevent the possibility of the overtopping, in the case of run-up, and the entrance of air inside the chamber to the submerged opening, in the case of run-down. In this case (wave with T = 9 s and H = 1.5 m), run-up and run-down amplitudes are 1.65 m and -1.26 m for wall slope of 40°, respectively, and 1.21 m and -0.80 m for 90°, respectively. Figure 10 shows run-up/down amplitudes (H_{run}) of different incident wave periods and H = 1.5 m and wall slopes of 40° and 90°. For wall slope of 40°, H_{run} decreases with the increase of the wave period and the maximum value occurs at T = 6 s. For wall slope of 90°, H_{run} has lower variation along the wave periods. These results infer that the possibility to occur overtopping or the air entrance into the chamber decrease to low wave periods in for wall slope of 40°. It is important emphasizing that these possibilities are expected more probable for higher wave heights.

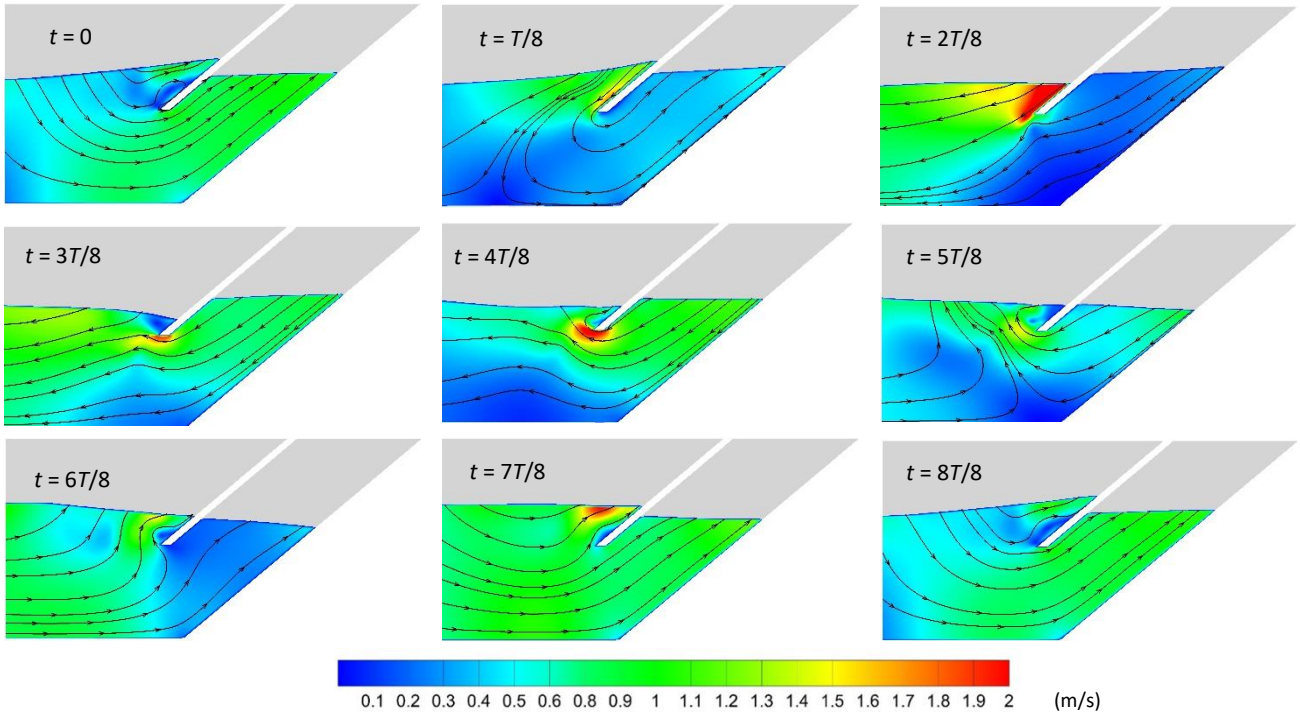

Figure 6. Contours of velocity magnitudes and streamlines around the chamber with wall slope of 40° and an incident wave of T = 9 s and H = 1.5 m.

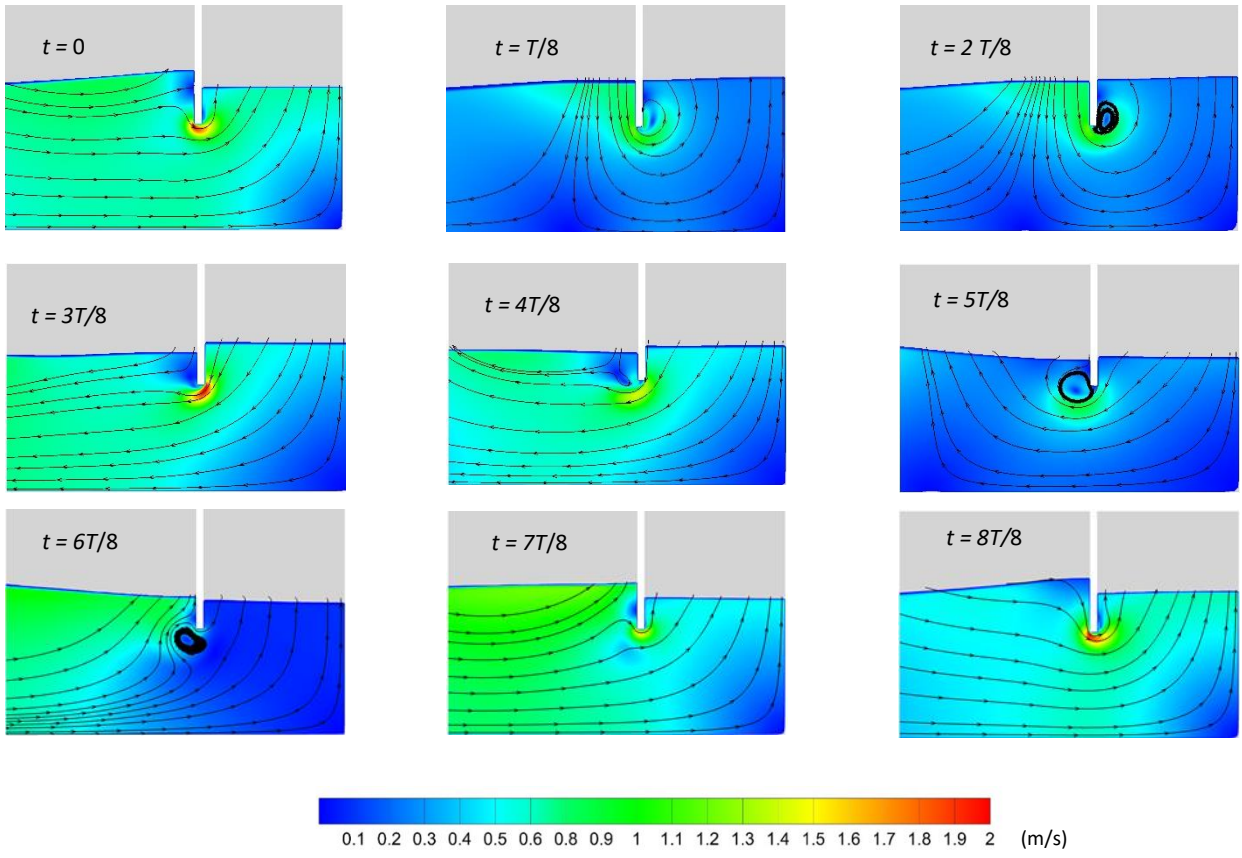

Figure 7. Contours of velocity magnitudes and streamlines around the chamber with wall slope of 90° and an incident wave of T = 9 s and H = 1.5 m.

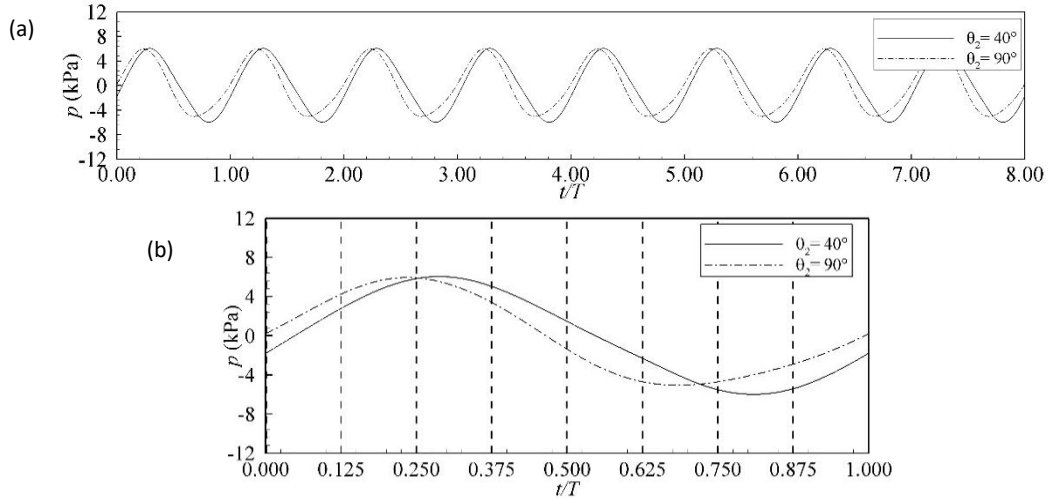

Figure 8. Time series of the air pressure inside the chamber with wall slopes of 40° and 90°, for an incident wave with *T* = 9 s and *H* = 1.5 m. **(a)** along 8 wave cycles; **(b)** along one wave period.

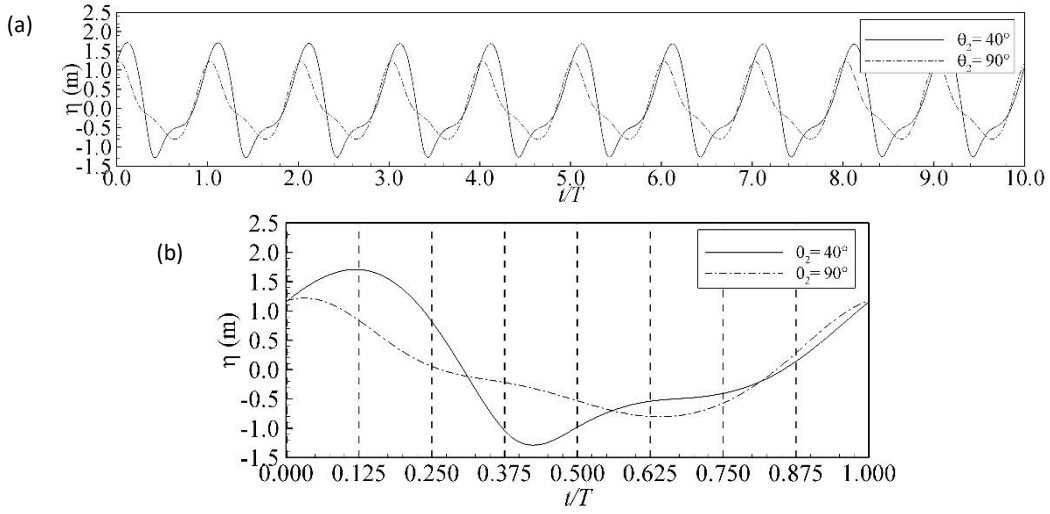

Figure 9. Time series of free surface elevation on the external surface of the frontal wall with slopes of 40° and 90° for an incident wave with *T* = 9 s e *H* = 1.5 m. **(a)** along 8 wave cycles; **(b)** along one wave period.

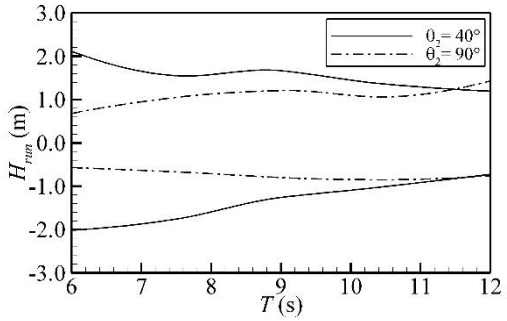

Figure 10. Run-up/down heights versus the wave period of the incident wave with *H* = 1.5 m and wall slopes of 40° and 90°.

Figure 11 shows time series of the free surface elevation at two gauges (GWA1 and GWA2) inside the chamber near the front and rear walls for wall slopes of 40°and 90 ° and an incident wave of *T* = 9 s and *H* = 1.5 m. For walls slope of 40° (shown in Figure 11 (a), (b)), the amplitude of the free surface elevation near the rear wall is higher than that of frontal wall, as expected. At *t = 2T/8*, during exhalation, the free surface elevations are 1.26 m and 0.67 m at the rear and the frontal walls, respectively. During the inhalation, at *t = 6T/*8, these values are -1.13 m and -0.42 m, respectively. The averaged differences of free surface elevation inside the chamber are 0.59 m and -0.71 m for exhalation and inhalation, respectively. This movement can be considered a shoaling phenomenon inside the

chamber, which, although natural, does not contribute to the pneumatic power generation. For walls slope of 90° (shown in Figure 11 (c), (d)), this phenomenon does not occur with the same intensity, in which the averaged differences of free surface elevation inside the chamber are around 0.10 m.

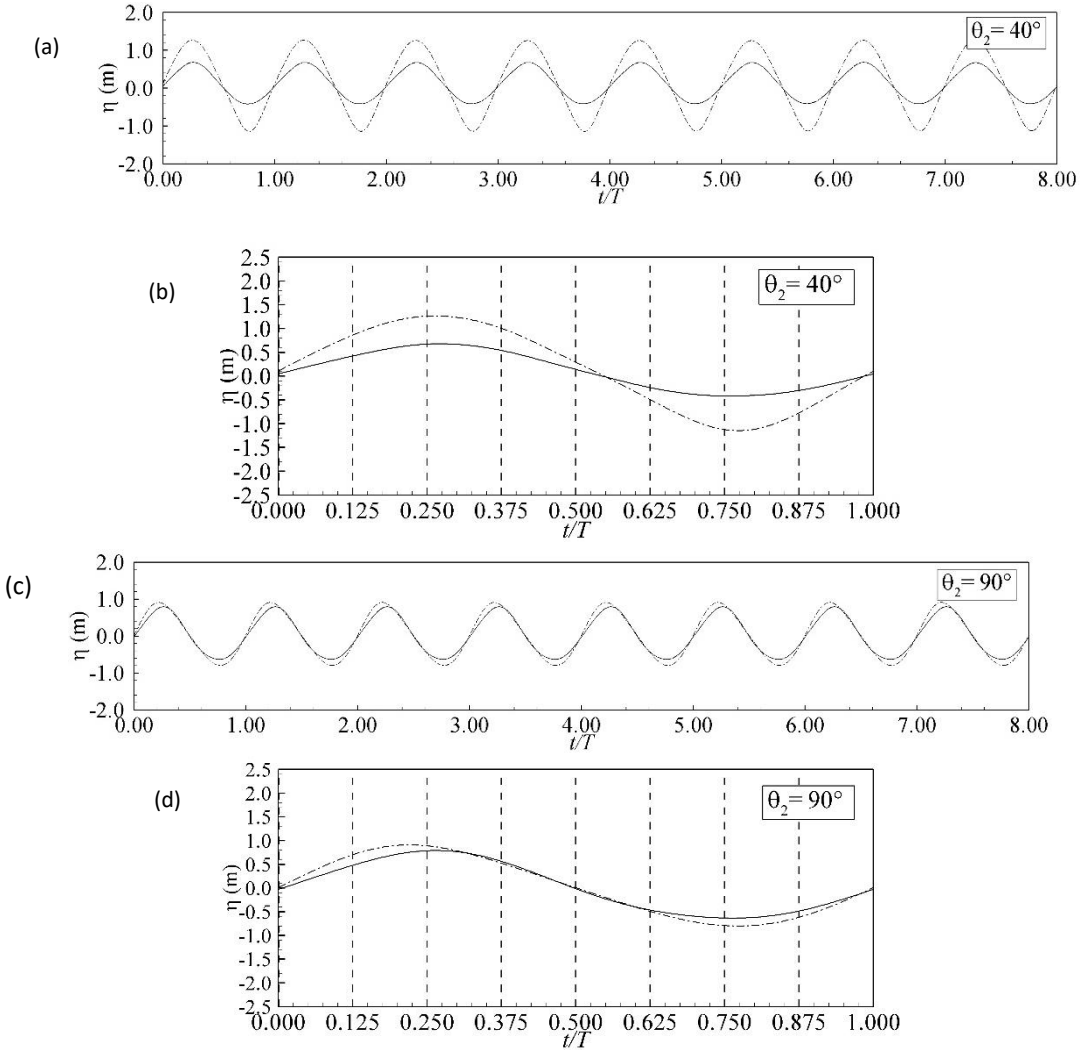

Figure 11. Time series of the free surface at two gauges inside the chamber near of the frontal wall GWA1 (solid line) and near the rear wall GWA2 (dashed line) for wall slopes of 40° and 90°, the incident wave of *T* = 9 s and *H* = 1.5 m. **(a)** and **(c)** along 8 wave cycles; **(b)** and **(d)** along one wave period.

Figure 12 shows time series of the free elevation at three gauges used to determine the reflection coefficient (GR1, GR2 and GR3) and of the incident and reflected waves, separated by using the algorithm developed by Souza et al. (2011). Although the time series of the free surfaces show some nonlinearity, it can be noticed that the incident wave has the similar height of that imposed by the wave-maker and a more intense nonlinearity of the reflected wave. In the case of wall slope of 40° the reflected height is (0.62 m), and for wall slope 90° is higher (0.74 m).

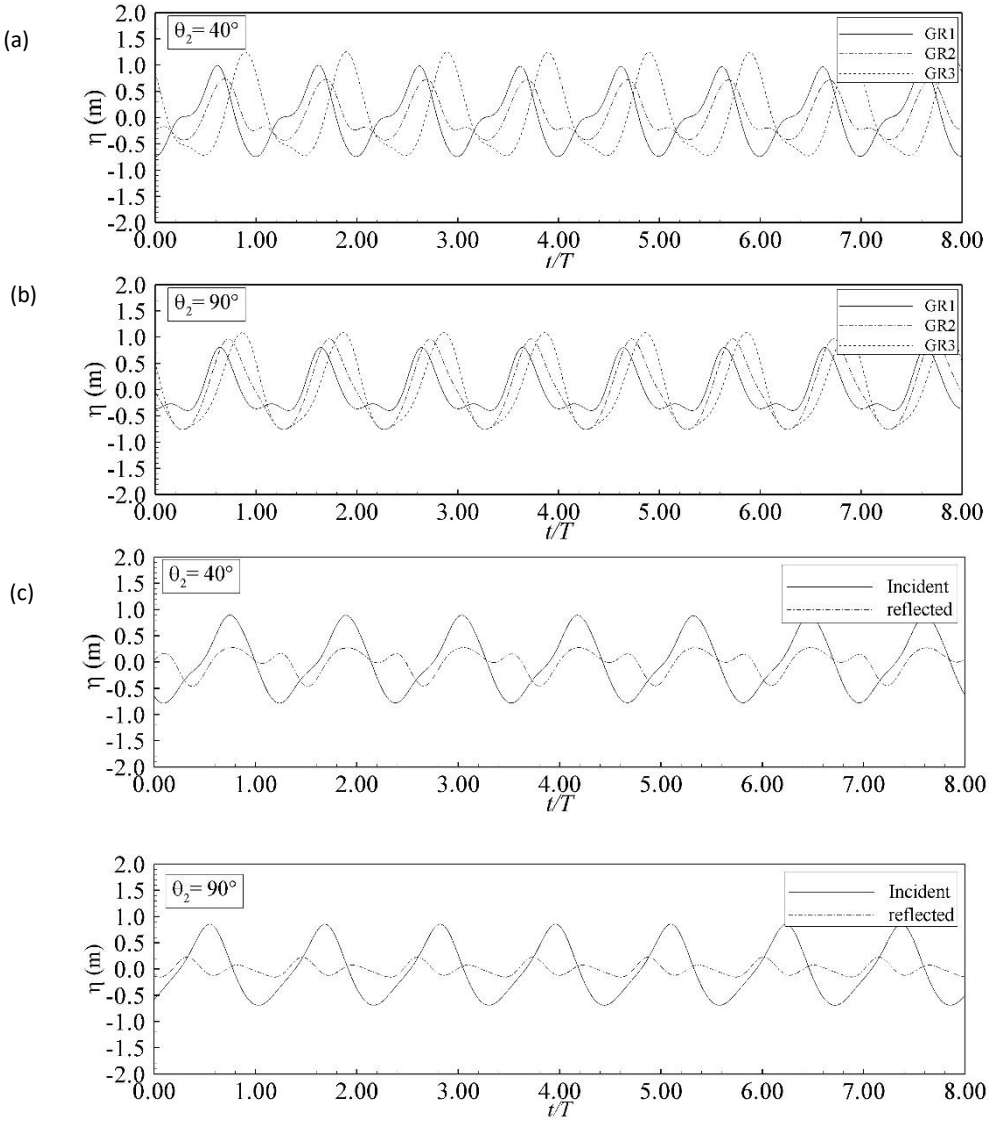

Figu ime series of the free surface elevation **(a)** and **(b)** at gauges GR1, GR 2 and GR 3; **(c)** and **(d)** of incident and reflected waves, for wall slopes of 40° and 90° for an incident wave of T = 9 s e H = 1.5 m.

The reflection coefficients (C_R) in relation to the wave period for the chamber with wall slopes of 40° and 90° are shown in Figure 13. The maximum coefficient occurs at T = 12 s (around 0.50) and the minimum one at period 7.5 s, that is 0.31 and 0.21 for wall slopes of 40° and 90°, respectively. At period of 6 s, the wall slope of 90° had a C_R lower than that of 40°.

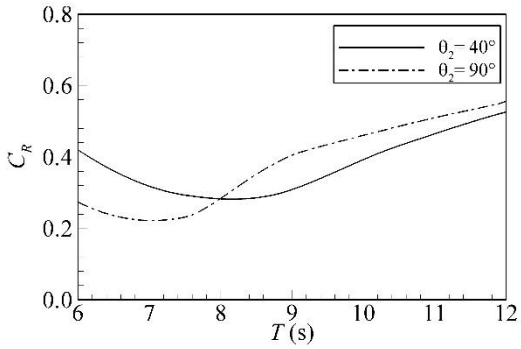

Figure 13. Reflection coefficient in relation to the wave period for chambers with wall slopes of 40°.

3.3 Energy balance around the OWC device

In this Section, an energy balance is carried out to quantify types of energy distributed by the wave energy input into the flume. Figure 14 shows the reflected energy (*ER*/*EI*) and energy losses (*ER*/*EI*) in relation to the wave energy for chambers with different wall slopes. In general, *ER*/*EI* tends to increase with the increase of the wave period; the maximum values are around 30% at *T* = 12 s. The minimum values of *ER*/*EI* occurs around *T* = 7.5 s (below 10%) for all wall slopes. The chamber will wall slope of 40° has lower *ER*/*EI* for periods from *T* = 7.5 to 12 s in relation to others. In general, waves with lower periods have higher energy losses *EL*/*EE*. Besides, *EL*/*EE* decreases with the increase of the wave period for all wall slopes. It can be noticed that *EL*/*EE* of *T* = 7.5, 9 and 10.5 s are similar for all wall slopes and the higher differences are at the limits of the range (*T* = 6 and 12 s), in which the wall slope of 40° shows the higher values. Different from *ER*/*EI*, minimum values of *EL*/*EE* occur around *T* = 10.5 s for all wall slopes.

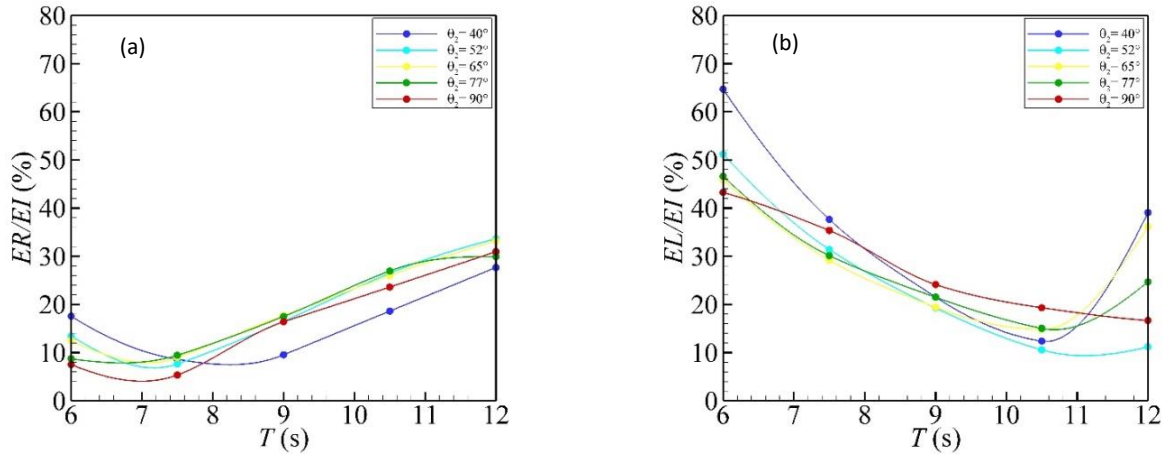

Figure 14. (a) Reflected energy (*ER*/*EI*) and **(b)** energy losses (*EL*/*EI*) related to the wave energy versus wave period for chambers with different wall slopes.

Figure 15 shows *EE*/*EI* in relation to the wave period for different chamber wall slopes. Highest values of *EE*/*EI* = 60% occur at periods from *T* = 7.5 to 10.5 s for all cases, except with wall slope of 40°. The latter case has the maximum *EE*/*EI* of 70% from *T* = 9 to 10.5 s. In all cases, lower values occurs at *T* = 6 and 12 s (minimum of 18% at *T* = 6 s for 40°). Although the chamber with wall slope of 40° has higher extracted energy, the case with wall slope of 90° shows lower variation in the range of the wave period, which is a good characteristic, considering the natural variability of the wave period of a sea state.

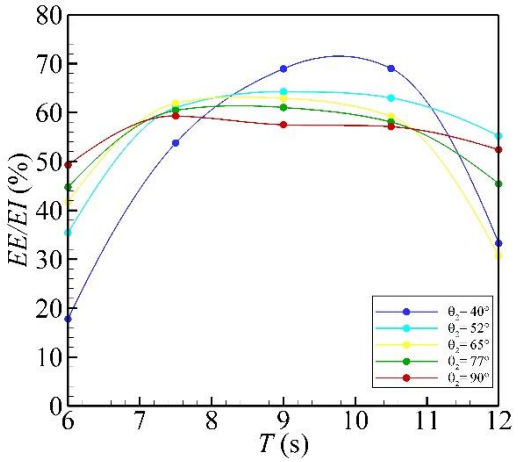

Figure 15. Extracted energy related to the wave energy (*EE*/*EI*) versus wave period for chambers with different wall slopes.

4. Conclusions

In this study, numerical analysis of the hydro-pneumatic behavior of and the energy balance of OWC devices, with different wall slopes (from 40° to 90°) and Wells turbine (*kt* = 100 Pa.s.m^{-3}), subject to regular incident waves

(periods from 6 to 12 s) were carried out. Numerical simulations were performed by means of the FLUENT® software, which is based on RANS equations.

Firstly, the wave propagation in the numerical flume of a wave with T = 9 s and H = 1.5 m was verified and results of time series of free surface elevations of several gauges along the flume showed the good accuracy of the implemented methodology. Afterwards, analyses of the hydro-pneumatic behavior of OWC devices with wall slopes of 40^{o} and 90^{o} (vertical) due to an incident wave of T = 9 s and H = 1.5 m were carried out. Contours of velocity magnitude and gauge measures allowed the observation of main phenomena during the wave-structure interaction. The highest velocity magnitudes occurred at external surface of the front wall, during wave run-up/down, and on the corner of the lip at different instants. Run-up/down phenomena were more significant for chamber wall slope of 40^{o}; however, considering the characteristic of the incident waves, neither entrance of the air inside the chamber nor the overtopping occurred. It is important emphasizing that extreme waves of the sea state must be tested for OWC design proposals. Another important phenomenon was the sloshing inside the chamber, in which the free surface experiments oscillations between the walls. This phenomenon was more significant for wall slope of 40^{o}, as expected; free surface near the rear wall had higher amplitudes than the ones of near the front wall. Measurement of reflected waves showed that chamber wall slope of 90^{o} showed higher reflected coefficients in relation to 40^{o} at wave periods higher than 7.5 s.

Analysis of the energy balance showed that the chamber with wall slope of 40^{o} reached the highest extracted energy at wave periods of 9 and 10.5 s, with *EE*/*EI* of 70%; however, at the other periods this case had the lowest one, caused mainly by the high values of energy losses (*EL*/*EI*). Although the chamber with wall slope of 90^{o} did not show highest values of *EE/EI* (maximum of 59%), this case had lower differences of *EE*/*EI* at the range of wave periods. These analyses showed that chambers with lower wall slopes allow higher extracted energy at wave periods from 7.5 to 10.5 s; however, this energy decay significantly at other wave periods. Therefore, the choice of the optimal chamber wall slope depends on the sea state characteristics. Besides, this investigation allowed understanding the importance of analyzing the run-up/down on the front wall and sloshing inside the chamber in the OWC design.

References

1. Conde, J.M.P.; Teixeira, P.R.F.; Didier, E. Numerical simulation of an oscillating water column wave energy converter: comparison of two numerical code. In: Proceedings of the 21th International Offshore and Polar Engineering Conference, Maui, 2011; pp. 688-674.
2. Costa, R.S.; Lima, F.J.L.D.; Rüther, R.; Abreu, S.L.D.; Tiepolo, G.M.; Pereira, S.V.; Souza, J.G.D. *Atlas Brasileiro de Energia Solar*, 2ª ed.: INPE. São José dos Campos – SP, 2017 (in Portuguese).
3. Dean, R.G.; Dalrymple, R.A. *Water wave mechanics for engineers and scientists. First Published in 1984 by Prentice Hall*, Inc. World scientific publishing Co. Pte. Ltd., London, 2000.
4. Dias, J.; Mendonça, A.; Didier, E.; Neves, M.G.; Conde, J.M.P.; Teixeira, P.R.F. Application of URANS-VOF models in hydrodynamics study of oscillating water column. In: Proceedings of SCACR2015 - International Short Course/Conference on Applied Coastal Research, Florence, Italy, 2015.
5. Didier, E.; Teixeira, P.R.F.; Neves, M.G. A 3D Numerical Wave Tank for Coastal Engineering Studies. *Defect and diffusion forum*: **2016**, *volume* 372, pp. 1-10.
6. Elhanafi, A.; Fleming, A.; Macfarlane, G.; Leong, Z. Numerical energy balance analysis for an onshore oscillating water column wave energy converter. *Enegry* **2016**, *volume* 116, pp. 539-557.
7. Falcão, A.F. Control of an oscillating-water-column wave power plant for maximum energy production. Applied *Ocean Research* **2002**, *volume* 24, n. 2, pp. 73-82.
8. FLUENT, 2016. User's Guide. ANSYS Inc.
9. Folley, M.; Whittaker, T. Identification of non-linear flow characteristics of the LIMPET shoreline OWC. In. Proceedings of The Twelfth International Offshore and Polar Engineering Conference. Kitakyushu, Japan, 2002.
10. Gaspar, A.L.; Teixeira, P.R.F.; Didier, E. Numerical analysis of the performance of two onshore oscillating water column wave energy converters at different chamber wall slopes. *Ocean Eng*. **2020**, *volume* 201, №107119.
11. IEA (International Energy Agency) Key World Energy Statistics 2020. Available in :< http://energyatlas.iea.org/#!/tellmap/-1118783123> Access in Dec. 2020.
12. Lagoun, M.S.; Benalia, A.; Benbouzid, M.E.H. Ocean Wave Converters: State of the Art and Current Status. In Proceedings of International Energy Conference, IEEE 2010. Manama, Bahrain, 2010, pp. 636-641.

13. Lisboa, R.C. Avaliação Numérica da Potência das Ondas Absorvida por um Dispositivo de Coluna de Água Oscilante Instalado na Costa Sul do Brasil. Dissertação de Mestrado em Engenharia Oceânica, Universidade Federal do Rio Grande, 2016 (in Portuguese).
14. Mansard, E.P.D.; Funke, E.R. The Measurement of Incident and Reflected Spectra Using a least Squares Method. *Coast. Eng*. **1980**, *volume* 4, pp.154-174.
15. Mendonça, A.; DIAS, J.; Didier, E.; Fortes, C.J.E.M.; Neves, M.G.; Reis, M.T.; Conde, J.M.P.; Poseiro, P.; Teixeira, P.R.F. An integrated tool for modelling OWCWECs in vertical breakwaters: preliminary developments. *J. Hydro-environ*. **2018** , pp.198-213.
16. Mørk, G.; Barstow, S.; Kabuth, A.; Pontes M.T. Assessing the global wave energy potential. In: Proceedings of the International Conference on Offshore Mechanics and Arctic Engineering - OMAE, Shanghai, China, 2010; ed. 3, p. 447-454.
17. Scäffer, H.A.; Klopman, G. Review of multidirectional active wave absorption methods. J. Waterw. Port, *Coast*. *Ocean Eng*. **2000**, *volume* 126 (2), pp. 88-97.
18. Sousa, G.A.C.F.; Neves, M.G.; Capitao, R. Separação de agitação incidente e reflectida: testes comparativos. In: Proceedings of 7ªs Jornadas Portuguesas de Engenharia Costeira e Portuária, AIPCN-PIANC, 2011 (in Portuguese).
19. Teixeira, P.R.F.; Davyt, D.P.; Didier, E.; Ramalhais, R. Numerical simulation of an oscillating water column device using a code based on Navier-Stokes equations. *Energy* **2013**, *volume* 61, pp. 513-530.
20. Torres, F. R.; Teixeira, P.R.F.; Didier, E. Study of the turbine power output of an oscillating water column device by using a hydrodynamic - aerodynamic coupled model. *Ocean Eng*. **2016**, *volume* 125, pp. 147–154.
21. Tseng, R.S.; Wu, R.H.; Huang, C.C; Model study of a shoreline wave-power system. *Ocean Eng*. **2000**, *volume* 27, pp. 801–821.
22. Versteeg, H.K.; Malalasekera, W. *An Introduction to Computational Fluid Dynamics*, Longman, Malasia, 1999, pp. 257.